Springer Acta Mechanica Sinica

•RESEARCH PAPER•

Acta Mech. Sin., Vol. 38, 322057 (2022)
https://doi.org/10.1007/s10409-022-22057-x

Hydroelastic responses of an elastic cylinder impacting on the free surface by MPS-FEM coupled method

Congyi Huang, Guanyu Zhang, and Decheng Wan*

Computational Marine Hydrodynamics Lab, School of Naval Architecture, Ocean and Civil Engineering, Shanghai Jiao Tong University, Shanghai 200240, China

Received July 5, 2022; accepted July 15, 2022; published online September 8, 2022

In naval engineering and offshore industry, the fluid-structure interaction (FSI) problem is a very common problem, and water entry is a very representative one. The hydroelasticity effects due to slamming are of great interest. In this paper, the water entry problem is simulated by the moving particle semi-implicit & finite element method (MPS-FEM) coupled method. The MPS method is used for the fluid because it is very suitable for the violent free-surface flow. The structure domain is solved by the FEM method because of the maturity in solving structural motion and deformation. The water entry of a rigid cylinder is numerically studied first and the results show good agreements with previous published data. After that, variable analysis is conducted in the water entry simulation of an elastic cylinder, including the structural elasticity and impact velocity.

Moving particle semi-implicit method, Finite element method, Fluid-structure interaction, Water entry, MPSFSI solver

Citation: C. Huang, G. Zhang, and D. Wan, Hydroelastic responses of an elastic cylinder impacting on the free surface by MPS-FEM coupled method, Acta Mech. Sin. **38**, 322057 (2022), https://doi.org/10.1007/s10409-022-22057-x

1. Introduction

Water entry is a typical fluid-structure interaction (FSI) phenomenon, such as the high-speed vessels impacting with water and the seaplane landing on the sea. In such cases, the structures may deform, and thus the interactions between the fluid and the structure may be involved. Under the great impacting loads, the trajectory of structures will be affected, and local deformations or even damages dramatically increase. Therefore, the hydroelastic responses of the elastic structures due to the fluid impact loads become of paramount importance in practical engineering problems.

Until now, many scholars concentrate on the water entry problems through a variety of methods. There are mainly three ways to study this problem: experimental analysis, theoretical solutions and numerical simulations. Experimental analysis is the main approach by early researchers to investigate water entry problems. The movement track of structures can be captured by high-speed cameras. Greenhow and Lin [1] designed an experiment to investigate the wedge and cylinder entering the water. Shibue et al. [2] carried out experimental work on water entry of elastic cylindrical shell, and measured the impact pressure and structural strain response of the cylinder shell during water entry. In terms of analytical solutions, Scolan [3] developed the semi-analytical solution of elastic wedge impacting on the free surface based on Wagner theory and the linear elastic model. Sun and Faltinsen [4] carried out the numerical simulation of water slamming of an elastic cylindrical shell based on boundary element method (BEM) method and modal superposition method, and the obtained structural strain response was generally consistent with the experimental results of Shibue et al. [2]. Yu et al. [5] analyzed the elastic wedge body using the semi-analytical hydrodynamic impact theory and the pressure on the wedge surface was calculated by the Wagner theory. Zhang et al. [6] combined the modal superposition method, BEM and Wagner theory, to study the slamming problem of an elastic wedge.

Recently, with the development of high-performance parallel computing technology, researchers develop various

*Corresponding author. E-mail address: dcwan@sjtu.edu.cn (Decheng Wan)
Executive Editor: Yue Yang

computational fluid dynamics (CFD) solver to investigate the water entry problems. Zhu et al. [7] combined the Eulerian mesh-based solvers with the constrained interpolation profile (CIP) method to simulate the water entry of a rigid circular cylinder. Qu et al. [8] conducted numerical simulations on the water entry of an elastic cylinder by the finite volume method (FVM) and finite element method (FEM) coupled method. Through numerical simulation, the impact characteristics of rigid body and elastic body are analyzed, and the effects of structural stiffness, shell thickness and shell falling velocity on impact characteristics are studied. The above research all adopted the mesh-based method. When the free surfaces deform severely, the mesh may break up, which requires the mesh reconstruction and consume a lot of time.

There are some kinds of meshless approaches that are different from the mesh-based approaches mentioned above. The continuum is discretized into moving particles for the meshless methods, so that the calculation of the numerical dissipation of the convection term is avoided. In addition, it is easy to capture the free surface for the mesh-free methods due to the inherent Lagrange properties, and the treatment of mesh is avoided. Thus, the particle method is suitable for the problems with moving boundaries and the problems with free surface severe deformation. Therefore, particle methods have been widely used in solving FSI problems. At present, particle methods that are used widely include smoothed particle hydrodynamics (SPH) [9], moving particle semi-implicit method (MPS) [10], e.g., Refs. [11-14].

Lee et al. [15] simulated the water entry problem of an inclined plate through MPS method. Zhang et al. [16] simulated the water entry of two-dimensional (2D) wedges with different deadrise angles using MPS method. The numerical trajectory of the structure was consistent with the experiment. Tang et al. [17] combined the MPS method with multi-resolution particle technology to simulate the water entry of 2D cylinders, and the results agreed well with the experimental results [1]. Sun et al. [18] based on SPH method applied particle shifting technique (PST) to the fluid-rigid interface and corrected the non-physical interface separation phenomenon in the simulation of water entry. Some scholars considered the influence of gas phase in the water entry process based on the particle method. Khayyer and Gotoh [19] used WCMPS (Wake Compressible-MPS) method to study the water entry of a plate. The calculated results of multiphase flow were closer to the experimental data. Yan et al. [20] used the two-phase SPH method to simulate the water entry of a wedge. The results show that air-phase had little effect on the acceleration and impact pressure of the free-falling wedge. Many scholars consider the influence of structural response in water entry problem based on the particle method, such as pure particle method and particle method combined with other numerical methods. For instance, many scholars investigated the model proposed by Scolan [3] using the particle method [21-26]. Hwang et al. [21] used MPS method, and the impact pressure obtained presented obvious oscillation phenomenon, and the structural deformation was a little larger than the analytical solution. Khayyer et al. [22,23] used MPS-Hamiltonian MPS (MPS-HMPS) method and Incompressible SPH-SPH (ISPH-SPH) method to reproduce the model. It can be found that the advanced flow field solution method and structure solution method play a significant role in improving the calculation accuracy. Subsequently, Khayyer et al. [25] extended MPS-HMPS method into three-dimensional (3D) model and conducted the simulation of the water entry problem, and the results agreed well with the analytical solution. Khayyer et al. [27] simulated the water slamming on a sandwich hull based on ISPH-HSPH method, and the results consisted well with the theoretical solutions of Qin and Batra [28]. Lu et al. [29] simulated a 2D marine panel impacting into water by MPS-FEM method. Sun et al. [30] used the MPS-modal superposition method to simulate the water entry of an elastic cylinder shell, and the numerical strain agreed well with the experiment by Shibue et al. [2].

In this paper, the water entry of the elastic structures is simulated based on MPS-FEM coupled method using the in-house MPSFSI solver. There are some challenges in the data exchange process because of the isomerous interface between the fluid domain and the structure domain. Many algorithms have been proposed to solve this problem. Fourey et al. [31] compared the accuracy and efficiency of conventional parallel staggered (CPS) algorithm and conventional sequential staggered algorithm (CSS) through a series of standard FSI benchmark cases in their study of SPH-FEM coupled method. The results show that CSS algorithm has higher stability for challenging FSI problems such as the FSI phenomenon with high-frequency vibration. It seems that CSS algorithm has become the primary choice for coupled methods. The information transformation at the fluid-solid interface has a direct impact on the accuracy and efficiency of the simulation. Mitsume et al. [32,33] applied MPS-FEM coupled method for FSI tests. A linear interpolation technology for exchange information is adopted. Fourey et al. [31] proposed the pressure integration scheme. The fluid particles in a certain range around the structural element are integrated. Zheng et al. [34,35] proposed the ghost cell boundary (GCB) model based on the MPS-FEM coupled method. In this model, the wall boundaries with complicated shapes can be dealt with FEM, and the interaction process is completed by the integration points of cells. Long et al. [36] coupled SPH method and FEM for solving FSI problems. An interface interpolation technology based on virtual particles was proposed.

In the previous research of our team [37,38], shape function based interpolation (SFBI) technique was proposed based on the interpolation characteristics of shape function in

FEM. And the kernel function based interpolation (KFBI) technique was proposed based on the interpolation characteristics of kernel function in MPS. The accuracy of the above two techniques has been validated by a series of FSI tests. In the process of implementation, it was found that the KFBI technique had less difficulty on arbitrary structural domain, which was extended to three dimensions lately [39].

In this paper, the MPS-FEM method is used to simulate the water entry of a 2D elastic circular cylinder. And coupling of MPS and FEM is accomplished by the CSS and KFBI technique. Firstly, the water entry of a rigid cylinder is simulated to validate the fluid solver. The reliability of MPS-FEM coupled method in simulating water entry of elastic body has been verified by simulating water entry of elastic marine panel [29]. In this paper, the deformation of elastic cylinder shell and the body trajectory of circular cylinder can be numerically obtained. It can be proved that the MPSFSI solver has good applicability when simulating the water entry problems of an elastic body. Two kinds of variables are investigated in the simulation of water entry of an elastic cylinder, including the structural elasticity and impact velocity. Through the detailed analysis of the numerical results, the mechanism of the water entry problem can be recognized.

2. Numerical methods

In this paper, the FSI problems are investigated by the MPS-FEM method. The fluid subdomain is solved by the MPS method, and the deformation and force of the structure are calculated by FEM.

2.1 Numerical method for fluid domain

In our previous papers, the MPS methods have been introduced in detail including the governing equations and boundary conditions (Zhang et al. [11]; Tang et al. [12]; Zhang and Wan [40]). In this section, the theories will be introduced briefly.

2.1.1 Governing equations

The governing equations of the fluid particles for MPS method are the continuity equation and momentum equation. And in the MPS method, the equations should be written in Lagrangian form, like Eqs. (1) and (2).

$$\nabla \cdot \mathbf{V} = 0, \tag{1}$$

$$\frac{\mathrm{D}\mathbf{V}}{\mathrm{D}t} = -\frac{1}{\rho}\nabla p + \nu \nabla^2 \mathbf{V} + \mathbf{g}. \tag{2}$$

As can be seen from the above formula, due to the Lagrange characteristics of MPS method, there is no convection term which exists in the mesh-based methods.

2.1.2 kernel function

In MPS method, the particles communicate with each other by the kernel function. Researchers have proposed various forms of kernel functions; and in this paper, an improved kernel function is used, which can be written as Eq. (3).

$$W(r) = \begin{cases} \dfrac{r_e}{0.85r + 0.15r_e} - 1, & 0 \le r < r_e, \\ 0, & r_e \le r. \end{cases} \tag{3}$$

It can be seen from Eq. (3) that when particle j is within the influence scope of particle i, the weight function of the influence of particle j on i is related to the distance between the two particles. When particle j is outside the influence scope of particle i, particle j has no effect on particle i. For different particle interaction models, the value of r_e is also different. It can be seen from the equation that when two particles are quite close, the kernel function value will not be too large because the denominator is not approximate to 0, which avoids the oscillation of the fluid pressure field and makes the calculation more stable.

2.1.3 Particle interaction models

In order to solve the governing equation, the velocity divergence $\nabla \cdot \mathbf{V}$, pressure gradient ∇p and other terms need to be discretized. This is accomplished by the interaction model between particles. The models used in this paper can be written as Eqs. (4)-(7).

$$\langle \nabla \phi \rangle_i = \frac{D}{n^0} \sum_{j \ne i} \frac{\phi_j + \phi_i}{\left|\mathbf{r}_j - \mathbf{r}_i\right|^2} (\mathbf{r}_j - \mathbf{r}_i) \cdot W\left(\left|\mathbf{r}_j - \mathbf{r}_i\right|\right), \tag{4}$$

$$\langle \nabla \cdot \mathbf{\Phi} \rangle_i = \frac{D}{n^0} \sum_{j \ne i} \frac{\left(\mathbf{\Phi}_j - \mathbf{\Phi}_i\right) \cdot (\mathbf{r}_j - \mathbf{r}_i)}{\left|\mathbf{r}_j - \mathbf{r}_i\right|^2} W\left(\left|\mathbf{r}_j - \mathbf{r}_i\right|\right), \tag{5}$$

$$\left\langle \nabla^2 \phi \right\rangle_i = \frac{2D}{n^0 \lambda} \sum_{j \ne i} \left(\phi_j - \phi_i\right) \cdot W\left(\left|\mathbf{r}_j - \mathbf{r}_i\right|\right), \tag{6}$$

$$\lambda = \frac{\sum_{j \ne i} W\left(\left|\mathbf{r}_j - \mathbf{r}_i\right|\right) \left|\mathbf{r}_j - \mathbf{r}_i\right|^2}{\sum_{j \ne i} W\left(\left|\mathbf{r}_j - \mathbf{r}_i\right|\right)}. \tag{7}$$

In the equations above, ϕ and $\mathbf{\Phi}$ represent arbitrary scalars and vectors respectively, D is the space dimensions number, $\mathbf{r}_{i,j}$ denotes the position of the particles, and n^0 is the initial particle number density. Table 1 shows the value of r_e in different particle interaction models, which is proposed by Koshizuka [10]. In Table 1, l_0 is the distance between two particles at initial time.

Table 1 The value of r_e in different particle interaction models

Particle interaction model	r_e
Gradient model	$r_{e\_\text{gra}} = 2.1l_0$
Divergence model	$r_{e\_\text{div}} = 2.1l_0$
Laplacian model	$r_{e\_\text{lap}} = 4.01l_0$

2.1.4 Pressure Poisson equation

In the MPS method, the pressure can be obtained by solving the pressure Poisson equation (PPE). Unlike the explicit method for solving the equation of state in the SPH method, this is a semi-implicit method. The PPE is solved by a mixed source term method, which was proposed by Tanaka and Masunaga [41] and Lee et al. [42]. The solution can be written as Eq. (8).

$$\left\langle \nabla^2 p^{k+1} \right\rangle_i = (1-\gamma)\frac{\rho}{\Delta t}\nabla \cdot V_i^* - \gamma\frac{\rho}{\Delta t^2}\frac{\left\langle n^k \right\rangle_i - n^0}{n^0}. \tag{8}$$

In Eq. (8), p^{k+1} and V_i^* represent the pressure at the time step $k+1$ and temporal velocity, respectively. γ is the weight parameter, and according to numerical experiments conducted by Lee et al. [42], the range of $0.01 \le \gamma \le 0.05$ is better. The value of γ is set to 0.01 in this paper. n^k is the temporal particle number density, and it is defined as the sum of the kernel functions of all particles in the support domain, which can be written as

$$\left\langle n^k \right\rangle_i = \sum_{j \ne i} W\left(\left|\mathbf{r}_j - \mathbf{r}_i\right|\right). \tag{9}$$

2.1.5 Free surface detection

Dirichlet boundary conditions need to be imposed on the free surface particles for solving the PPE. Therefore, detecting the free surface particles precisely is very important to accurately calculate the fluid pressure. In this paper, particle number density is used to find free surface particles. For the fluid internal particles, the support domain is usually full of particles. For the free surface particles, its support domain is always truncated, as shown in Fig. 1. When the particle number density satisfies the expression,

$$\left(\langle n \rangle_i / n^0\right) < 0.8. \tag{10}$$

It can be considered that the support domain of this particle is incomplete, so this particle can be judged as a free surface particle. When $\left(\langle n \rangle_i / n^0\right) > 0.97$, it can be considered that the support domain of this particle is full of particles, so the particle can be judged as a fluid internal particle. For the particle with number density, which satisfies the expression $0.8 < \left(\langle n \rangle_i / n^0\right) < 0.97$, additional judgment conditions need to be introduced.

There is another kind of detection method for surface particle [43] based on the asymmetry arrangement of neighbouring particles. And a vector function $\langle \mathbf{F} \rangle_i$ is introduced for this method, which can be written as Eq. (11).

$$\langle \mathbf{F} \rangle_i = \frac{D}{n^0}\sum_{j \ne i}\frac{\mathbf{r}_j - \mathbf{r}_i}{\left|\mathbf{r}_j - \mathbf{r}_i\right|} W\left(\left|\mathbf{r}_j - \mathbf{r}_i\right|\right). \tag{11}$$

The larger the value of $\langle \mathbf{F} \rangle_i$, the more asymmetric the distribution of neighbouring particles is. So the particles satisfying $\langle \mathbf{F} \rangle_i > 0.9|\mathbf{F}|^0$ can be judged as free surface particles, $|\mathbf{F}|^0$ is the initial value of the surface particles.

2.1.6 Boundary condition

The free surface boundary condition is one of the boundary conditions in MPS method. Once a particle is judged as a free surface particle, the pressure of which is set to zero. The solid boundary condition is another boundary condition, and the particle arrangement at the solid boundary is shown in Fig. 2. The solid boundary consists of multiple layers of particles, including one layer of wall particles and two layers of ghost particles. Wall particles can generate repulsive forces on fluid particles, and the function of the ghost particle is to complete the support domain of the fluid particles near the boundary to avoid the phenomenon that the influence domain of the fluid particle is truncated by the boundary. The pressure of the wall particles is calculated by the PPE as same as the fluid particles. And for the ghost particles, the pressure can be obtained by interpolation.

2.2 Numerical method for structure analysis

The structure domain is calculated by the FEM method. In

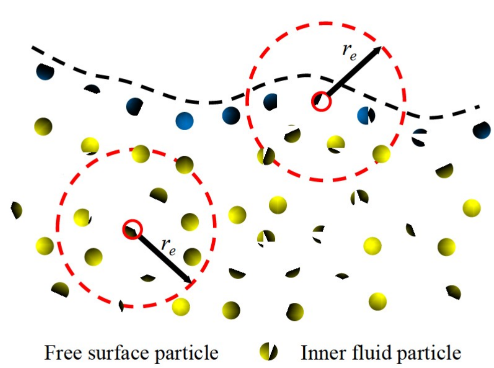

Figure 1 Schematic of free surface particle judgment.

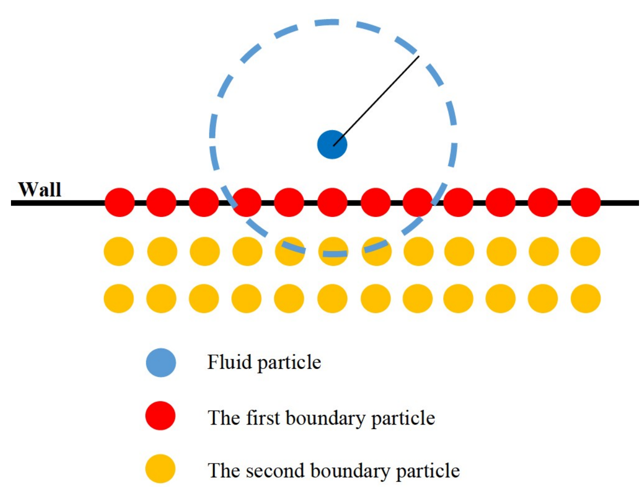

Figure 2 Diagram of muti-layer particle distribution.

this paper, the 2D plate element is used to discretize the structure. The governing equation is the dynamic balance equation of discrete elements, which are shown as Eqs. (12) and (13).

$$\mathbf{M}\ddot{y} + \mathbf{C}\dot{y} + \mathbf{K}y = \mathbf{F}, \tag{12}$$

$$\mathbf{C} = \beta_1\mathbf{M} + \beta_2\mathbf{K}. \tag{13}$$

In order to simplify the calculation process, Rayleigh damping matrix is used in this paper, as shown in Eq. (13). The damping matrix $\mathbf{C}$ can be expressed as a linear superposition of the mass matrix $\mathbf{M}$ and the stiffness matrix $\mathbf{K}$. By Taylor's expansion, the displacement of the node at the next time step can be obtained, as shown in Eqs. (14) and (15)[44].

$$\dot{y}_{t+\Delta t} = \dot{y}_t + (1-\gamma)\ddot{y}_t\Delta t + \gamma\ddot{y}_{t+\Delta t}\Delta t,\ 0 < \gamma < 1, \tag{14}$$

$$y_{t+\Delta t} = y_t + \dot{y}_t\Delta t + \frac{1-2\beta}{2}\ddot{y}_t\Delta t^2 + \beta\ddot{y}_{t+\Delta t}\Delta t^2, 0 < \beta < 1. \tag{15}$$

In this paper, the parameters in the above two equations are set to $\beta = 0.25$, $\gamma = 0.5$. Next, the governing equations of the structure domain can be solved, as shown in Eqs. (16)-(19) [45].

$$\overline{\mathbf{K}}y_{t+\Delta t} = \overline{\mathbf{F}}_{t+\Delta t}, \tag{16}$$

$$\overline{\mathbf{K}} = \mathbf{K} + a_0\mathbf{M} + a_1\mathbf{C}, \tag{17}$$

$$\begin{aligned}\overline{\mathbf{F}}_{t+\Delta t} = {} & \mathbf{F}_t + \mathbf{M}(a_0y_t + a_2\dot{y}_t + a_3\ddot{y}_t) \\ & +\mathbf{C}(a_1y_t + a_4\dot{y}_t + a_5\ddot{y}_t),\end{aligned} \tag{18}$$

$$\begin{aligned}& a_0 = \frac{1}{\beta\Delta t^2},\ a_1 = \frac{\gamma}{\beta\Delta t},\ a_2 = \frac{1}{\beta\Delta t},\ a_3 = \frac{1}{2\beta} - 1, \\ & a_4 = \frac{\gamma}{\beta} - 1,\ a_5 = \frac{\Delta t}{2}\left(\frac{\gamma}{\beta} - 2\right).\end{aligned} \tag{19}$$

2.3 Criteria for time steps

In MPS method, there are many kinds of criteria to help choose the appropriate time step for the fluid domain. Choosing the appropriate time step is very important for MPS method. If the time step is inappropriate, it may not only bring errors to the calculation results, but also cause instability and even failure of the calculation. In this paper, the time step is set by the Courant-Friedrichs-Lewy (CFL) condition, which can be written as Eq. (20).

$$\Delta t_f \le \frac{Cl_0}{u_{\max}}. \tag{20}$$

In Eq. (20), C denotes a parameter whose value is always set to 0-1.

For the structure domain, the time-step Δt_s for the FEM method should satisfy the central difference method, which can be written as Eqs. (21) and (22).

$$\Delta t_s \le \frac{L_{\min}}{C_s}, \tag{21}$$

$$C_s = \sqrt{\frac{E_s(1-\mu_s)}{\rho_s(1+\mu_s)(1-2\mu_s)}}\ . \tag{22}$$

In the equations above, E_s, μ_s and ρ_s denote the Young's modulus, Poisson's ratio, and density of structure. Obviously, in FSI solver, the time-step needs to meet both the requirements for the fluid and structure domain, which can be written as

$$\Delta t \le \min\left\{\Delta t_f, \Delta t_s\right\}. \tag{23}$$

For the relatively flexible structures considered in this paper, the time step for the structure is larger than that of the fluid domain. However, for the simulation between the stiff structure and fluid with high velocity, the time step for the structure would become smaller than that of the fluid domain. Therefore, when dealing with the FSI problem, the time step should be judged respectively according to the specific situation. Setting the time step properly can improve the efficiency and keep the calculation stable.

2.4 Coupling of MPS and FEM

As shown in Fig. 3, the coupling of MPS and FEM is realized by CSS method. In Fig. 3, $\mathbf{u}$ represents the velocity of the structure, and $\mathbf{p}$ denotes the pressure of fluid. Once the displacement and velocity of a structure node are known, we can get the velocity and the pressure by the fluid solver. Then load the pressure on the structure as the external force, we can get the new displacement and velocity by the structure solver. In the next step, these new structural nodal displacement and velocity can be used by the fluid solver.

The interface condition of displacement and traction equilibrium needs to be satisfied. Thus, an interface interpolation algorithm is employed, which can be written as Eqs. (24) and (25).

$$\mathbf{u}^F = \mathbf{u}^S, \tag{24}$$

$$p^F\mathbf{n}^F = -p^S\mathbf{n}^S. \tag{25}$$

$\mathbf{n}^S$ and $\mathbf{n}^F$ are normal vectors for interface particles in the structure and fluid domain, respectively. Then, the kernel function based interpolation (KFBI) technique is applied for the data interpolation. The displacement and the force are transformed between the fluid domain and the structure do-

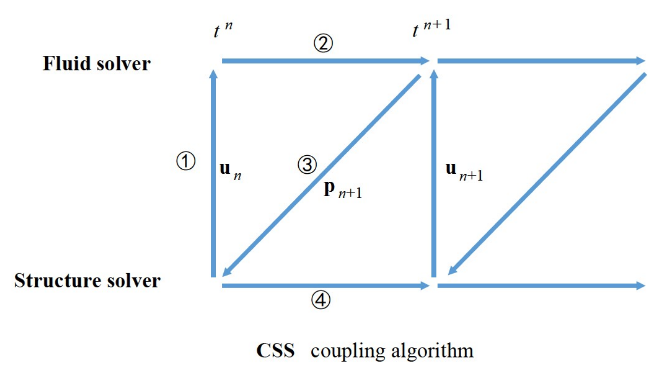

Figure 3 Schematic diagram of partitioned coupling strategy between fluid and structure field.

main in this process. The force transforms from fluid to the structure, and the displacement transforms from the structure to the fluid. The schematic diagrams of the transforms are shown in Figs. 4 and 5.

For structure node n, as shown in Fig. 4, the support domain of node n is a circle whose radius is the influence radius r_{e_i}. The boundary particles within the support domain are regarded as the neighbour particles of the structure node. The value of the influence radius r_{e_i} differs for distinct problems, and it is set to $0.5r_{e\_\mathrm{gra}} = 1.05l_0$ according to the previous research [38]. Then, the pressure at the structure node n can be estimated by the neighbour particles, which can be written as Eq. (26).

$$p_n^S = \frac{\sum_j p_j \cdot \mathbf{n}_j^F \cdot W\left(\left|\mathbf{r}_j - \mathbf{r}_n\right|\right)}{\sum_j W\left(\left|\mathbf{r}_j - \mathbf{r}_n\right|\right)}. \tag{26}$$

Figure 5 shows the displacement transformation. If the structure node is within the support domain of boundary particle, it will be considered as a neighbour node for the boundary particle. Then the displacement of boundary particle $\mathbf{w}_m^F$ can be obtained by weighted average of structural node displacement $\boldsymbol{\delta}_i$, which can be written as Eq. (27).

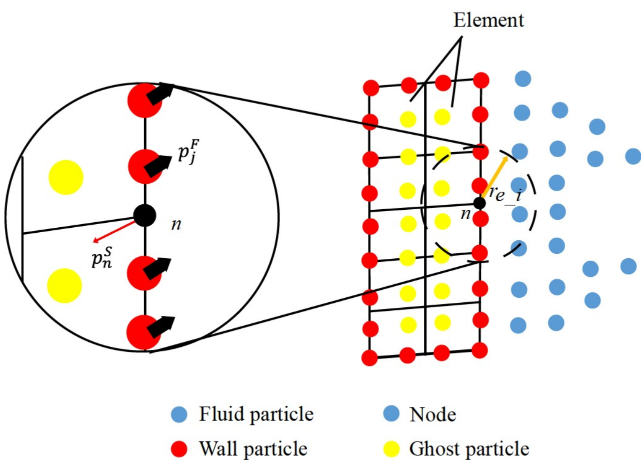

Figure 4 Schematic diagram of the force interpolation.

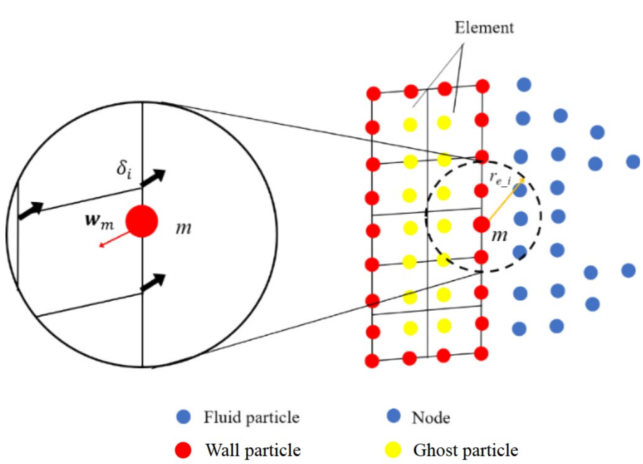

Figure 5 Schematic diagram of the displacement interpolation.

$$\mathbf{w}_m^F = \frac{\sum_i \boldsymbol{\delta}_i \cdot WW\left(\left|\mathbf{r}_i - \mathbf{r}_m\right|\right)}{\sum_i W\left(\left|\mathbf{r}_i - \mathbf{r}_m\right|\right)}. \tag{27}$$

3. Numerical simulations

3.1 Water entry simulation of a rigid cylinder

Firstly, the effect of structural elasticity is ignored. A rigid-body case is given to verify the accuracy of fluid solver. According to the experiment of Greenhow and Lin [1], the water entry process of a rigid cylinder is simulated. The sketch of the geometric model at the initial moment is shown in Fig. 6. The water depth d is 0.3 m, and a cylinder with a radius of $R = 0.055$ m is stationary above the still free surface of $H = 0.5$ m. When the cylinder impacts the water surface, the velocity is $V_0 = \sqrt{2g(H-R)} = 2.95$ m/s, where the acceleration of gravity is 9.81 m/s^2. In the experiment, two cylinders were chosen with weights equal to the whole and half of the buoyancy force applied to a completely submerged cylinder, which will be marked “neutral buoyant” and “half buoyant”, respectively. Detailed parameters of fluid field are shown in Table 2.

The penetration depths for both neutral and half buoyant cases are recorded, and the change with time is figured. The time-domain curves are compared with the results obtained by BEM [4] and the solutions recorded in the experiments [1], as shown in Fig. 7. The moment that the cylinder impacts onto the free surface is set as initial time. With gravity of

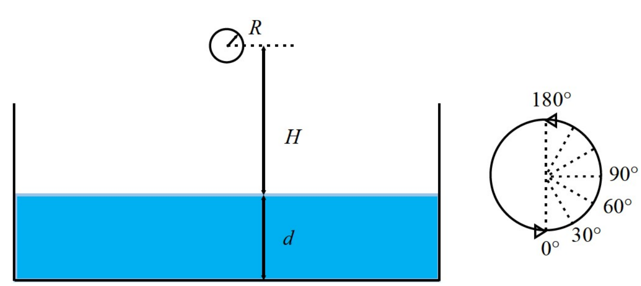

Figure 6 Geometric model of the rigid cylindrical shell on the still free surface.

Table 2 Calculation parameters value

Parameter	Value
Fluid density (water) (kg/m^3)	1000
Kinematic viscosity (m^2/s)	1.01×10^{-6}
Gravitational acceleration (m/s^2)	9.81
Water depth d (m)	0.3
Drop height H (m)	0.5
Outer radius R (m)	0.055
Particle spacing l_0 (m)	0.002
Total number	156567
Time step (s)	1×10^{-4}

cylinder and hydrodynamic force, the penetration depth of the cylinder increases gradually. The results obtained by the three different ways all agree well with each other according to Fig. 7. However, in the case of neutral buoyancy, there are significant differences between numerical results and experimental results. Greenhow and Lin [1] noted this apparent departure from mainstream trends and place a question mark in their report.

The free surface at typical time obtained by the present method is compared with experiment and BEM result, as shown in Fig. 8. For the half buoyant case, the cylinder falls from a height of 0.5 m above the still water surface and impacts on the water surface at about t = 0.301 s. When t = 0.305 s, the cylindrical shell contacts the water surface, and there is no obvious liquid splashing and separation phenomenon at this time. At t = 0.32-0.33 s, the wet surface of the structure increases rapidly, and the oblique upward jet on both sides of the cylinder appears, which is consistent with the experimental observation. At t = 0.385 s, the cylinder continues to move downward, and the V-shaped splashing jet is more significant. In the falling process of cylinder, the numerical free surface deformation is consistent with the experimental phenomenon. The same conclusion can also be obtained in the neutral buoyant case. In a word, the present method can be applied to simulate the water entering problem of rigid-body structure accurately.

3.2 Water entry simulation of an elastic cylinder

In this section, the influence of structural elasticity is con-

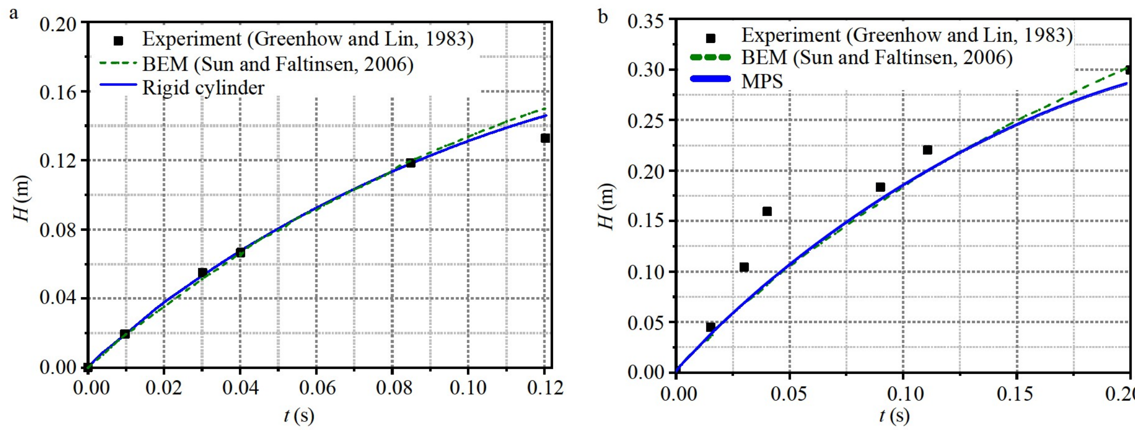

Figure 7 Time history curve of penetration depth for both cases. **a** Half buoyant case; **b** neutral buoyant case.

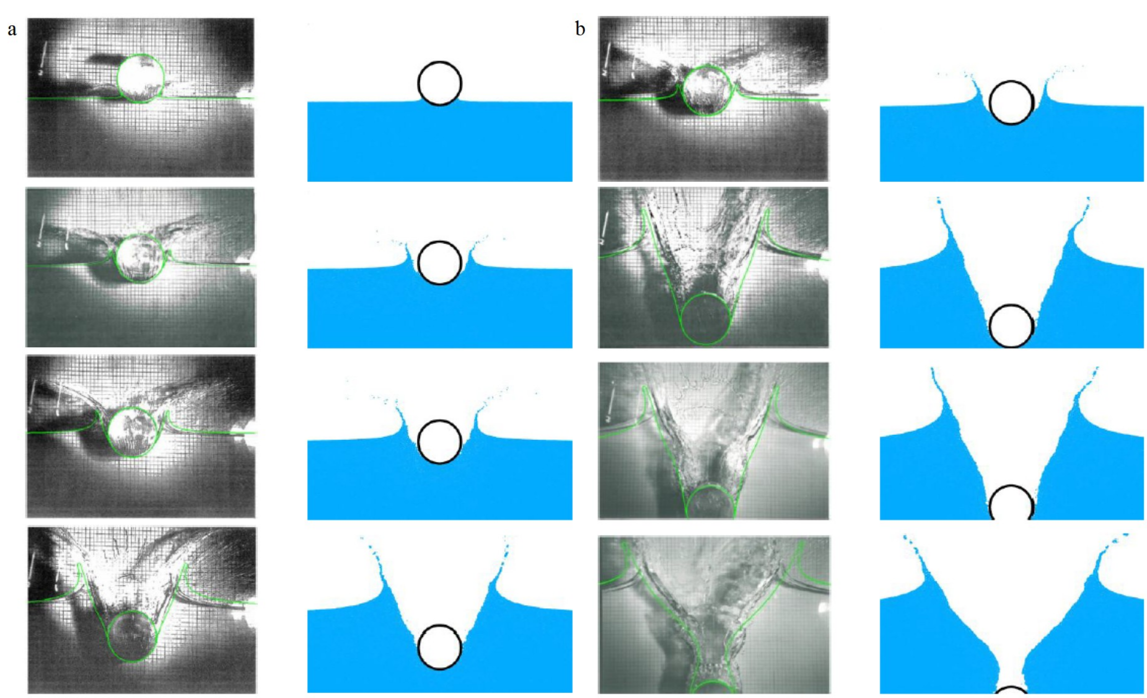

Figure 8 Free surface profiles during the falling process of cylinder in both cases. **a** Half buoyant case (t = 0.305 s, 0.320 s, 0.330 s, 0.385 s); **b** neutral buoyant case (t = 0.315 s, 0.390 s, 0.410 s, 0.500 s).

sidered. The water entry of a cylindrical shell is simulated through proposed MPS-FEM coupled method. Taking aforementioned experiment of Greenhow and Lin [1] as reference, three kinds of cylindrical shells are chosen, where one of these cylindrical shells is rigid-body and the other two are flexible-body with Young's modulus E_s of 1 GPa and 0.1 GPa. The outer diameter of the cylindrical shells is also set as 0.11 m. The weight of above two cylindrical shells is the same as that of the half buoyant case in the experiment. The detailed parameters in structure field are shown in Table 3.

Table 3 Calculation parameters of the cylinder

Parameter	Value
Solid density (kg/m^3)	7000
Young's modulus (GPa)	1/0.1
Outer radius R (m)	0.055
Shell thickness (m)	0.002
Poisson's ratio	0.34
Element type	Plane element
Element number	100
Interpolation effective radius r_{e_i} (m)	0.002

Figure 9 presents the particle model and element model in this case.

The free surface profiles at typical time instants obtained by the present method for the half buoyant case are shown in Fig. 10. In the case of elastic cylinder, stress occurs on the shell surface from the moment when the cylinder impacts onto the free surface. For the cylinder with the Young's modulus E_s = 1 GPa, there is no obvious deformation of the cylindrical shell, and the distributed stress becomes smaller with the increase of the penetration depth of the cylindrical shell. Meanwhile, the shape of the free surface is almost the same as that of the rigid-body. For the cylinder with the

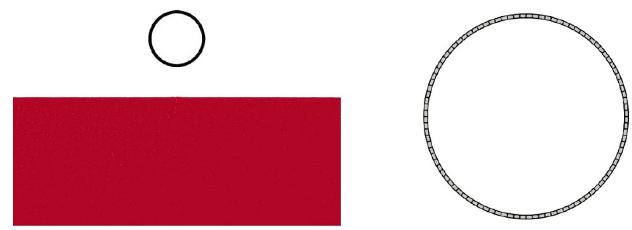

Figure 9 Particle model and element model.

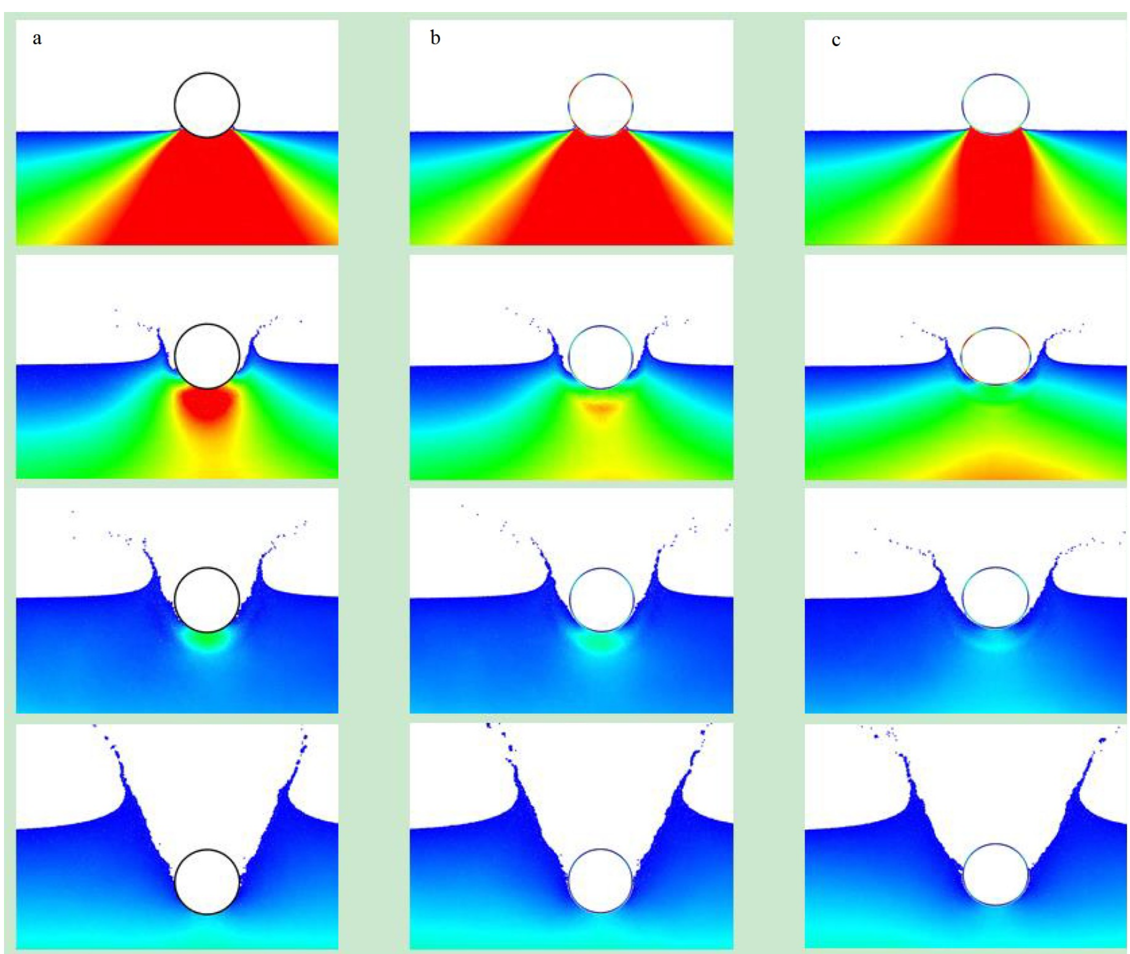

Figure 10 Pressure/stress fields during the elastic cylindrical shell impacting on still free surface (t = 0.305 s, 0.320 s, 0.330 s, 0.385 s). **a** Rigid; **b** E_s = 1 GPa; **c** E_s = 0.1 GPa.

Young's modulus E_s = 0.1 GPa, significant deformation of the cylindrical shell can be observed. At t = 0.305 s, the cylindrical shell compresses and deforms in the vertical direction under the violent collision with the free surface, and then the width increases in the horizontal direction. When t = 0.320 s, the deformation degree of cylinder increases, and the stress distribution also increases. As the penetration depth of cylindrical shell increases, the shell gradually returns to its original shape. Through comparison, it can be found that the shell deformation has a direct effect on the free surface deformation. In addition, at the initial stage of water entry, the contact surface is almost flat, and radiates outwards from the contact. Subsequently, the flow field pressure gradually returns to the hydrostatic pressure. In the process of water entry, the pressure field is symmetrically distributed relative to the cylinder, which has considerable stability. For the elastic cylinders, the pressure peak of the flow field is slightly smaller, and the cylinder with small Young's modulus forms a smaller range of shock wave, and the occurrence time is shorter.

The time history curves of the penetration depth for the two elastic cylinders are drawn and compared with that of the rigid cylinder, as shown in Fig. 11. It can be seen that the curve of the elastic cylinder with Young's modulus E_s = 1 GPa is almost as same as that of the rigid-body. For elastic cylinder with Young's modulus E_s = 0.1 GPa, the penetration depth is slightly less.

The deformation shape of the elastic cylinder at different times during the water entry is shown in Fig. 12. When t = 0.3 s, the cylinder did not impact on the free surface, and the cylinder presents no deformation at this time. Once the shell impacts onto the free surface, a huge vertical impact load is brought on the cylinder, and the pressure difference between the upper and lower sides of the cylinder is large, which makes the cylinder produce compression deformation in the vertical direction and tensile deformation in the horizontal direction. When the cylinder falls further, the pressure in the flow field returns to the hydrostatic pressure, and the cylinder gradually returns to its original shape and produces reverse deformation, and the cylinder compresses in the horizontal direction and stretches in the vertical direction. For the elastic cylinder with Young's modulus E_s = 1 GPa, the shell has the maximum deformation at 0°, 90°, 180° and 270°. However, the deformation is small. For the elastic cylinder with Young's modulus E_s = 0.1 GPa, the deformation process is obvious. From t = 0.3 to 0.465 s, the cylinder produces compression deformation in the vertical direction, and the deformation degree is the largest at t = 0.315. The maximum deformation can reach 6.4 mm at 90° and 270°. At t = 0.465 s, the cylinder returns to its original shape. Then, at t = 0.465-0.5 s, the cylinder has a slight reverse deformation, and the maximum deformation can reach 0.8 mm.

The effect of structural stiffness on the slamming force is discussed. Figure 13 shows the vertical force coefficients C_d

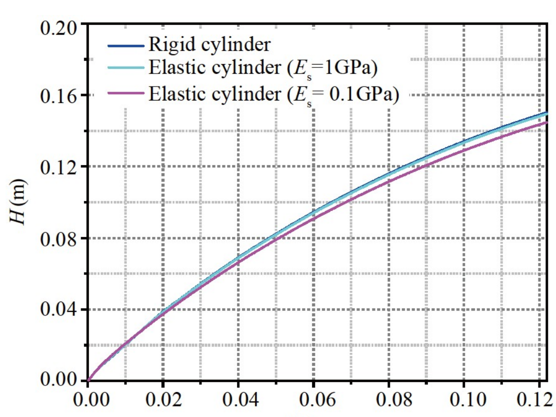

Figure 11 Time history curves of penetration depth.

a

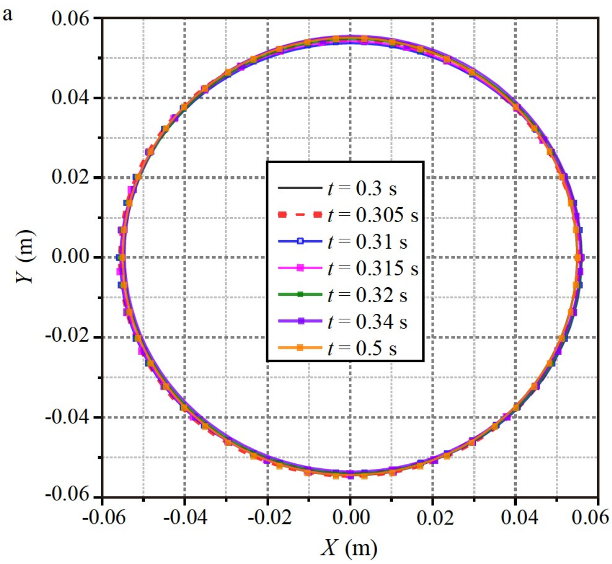

b

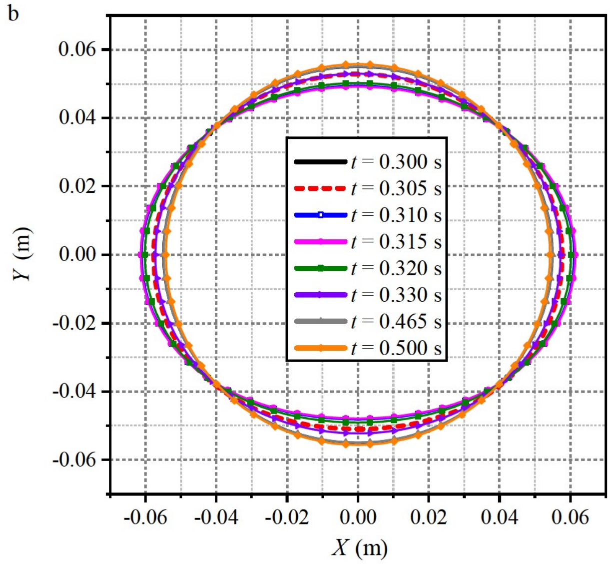

Figure 12 Deformation of the elastic cylinder. **a** E_s = 1 GPa; **b** E_s = 0.1 GPa.

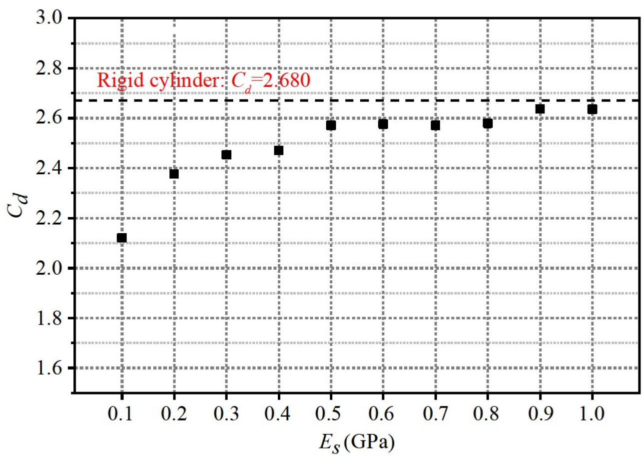

Figure 13 Vertical force coefficients versus Young's modulus.

versus Young's modulus. The vertical force coefficient of the rigid cylinder is given as a reference. It can be seen that the coefficient of C_d increases with the structural stiffness. When the structure stiffness is large, such as E_s of 0.9-1 GPa, the coefficient C_d is approximately close to that of the rigid-body.

3.3 The influence of impact velocity

In this section, the structural response characteristics at different impact velocities are investigated. The Young's modulus E_s is set as 1 GPa. The parameters of the cylinder are the same as in the previous section. Three kinds of drop heights are studied in this section, and the drop heights and corresponding impact velocities are shown in Table 4.

The deformation of the elastic cylinder with the impact velocity of 4.31 m/s is shown in Fig. 14. Compared with Fig. 12a, the deformation of the elastic cylinder becomes more obvious when the impact velocity increases.

The time histories of the cylinder diameter under different impact velocities are shown in Fig. 15. The moment that the cylinder impacts onto the free surface is set as initial time. By comparing the changing process of diameter, it can be determined that the peak value of the deformation increases with the increase of impact velocity. After that, the tendencies of the deformation under different impact velocities are consistent.

Table 4 The drop heights and corresponding impact velocities of the elastic cylindrical shell

Case	Drop height H (m)	Impact velocity V_0 (m/s)
Case 1	0.5	2.95
Case 2	0.6	3.27
Case 3	0.7	3.56
Case 4	0.8	3.82
Case 5	0.9	4.07
Case 6	1.0	4.31

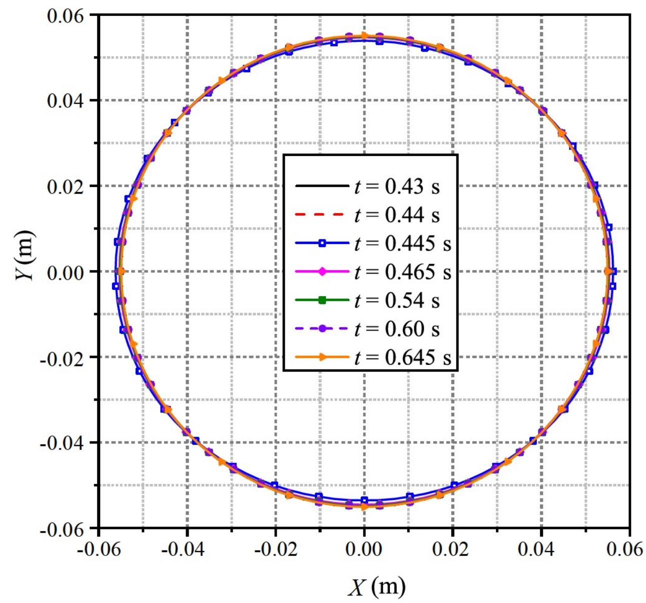

Figure 14 Deformation of the elastic cylinder (H = 1.0 m and V_0 = 4.31 m/s).

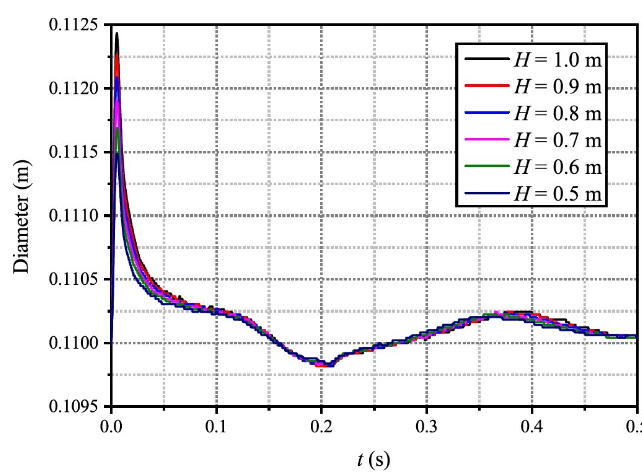

Figure 15 Time histories of the elastic cylinder diameter.

4. Conclusions

The water entry of the rigid and elastic cylinders is simulated, and the hydroelastic responses have been investigated by the MPS-FEM method in this paper. The fluid solver is first validated by simulating the water entry of the rigid cylinder, and a relatively good agreement is achieved between MPS result and published data. Then, two kinds of variables analysis are investigated in the simulation of water entry of elastic cylinder, including the structural elasticity and impact velocity. The deformation of shell and the body trajectory of circular cylinder can be obtained, so as to verify that the MPSFSI solver has good applicability in the simulation of the elastic body into water. Through the detailed analysis of the numerical results, the mechanism of the water entry problem is recognized.

Author contributions *Congyi Huang completed the debugging and validation of the software, designed the numerical simulation, completed the collation and visualization of the data, and wrote the paper. Guanyu Zhang helped complete the background investigation and software debugging and verification. Decheng Wan guided the concepts and methods of this article and completed the written review and editing.*

Acknowledgements *This work was supported by the National Key Research and Development Program of China (Grant No. 2019YFB1704200) and the National Natural Science Foundation of China (Grant Nos. 51879159 and 52131102).*

1 M. Greenhow, and W. M. Lin, Nonlinear Free Surface Effects: Experiments and Theory (Massachusetts Institute of Technology, Cambridge, 1983).
2 T. Shibue, A. Ito, and E. Nakayama, Structural response analysis of a cylinder under water impact, J. SNAJ Nihon Zousen Gakkai Ronbunshu **1993(174)**, 479 (1993).
3 Y. M. Scolan, Hydroelastic behaviour of a conical shell impacting on a quiescent-free surface of an incompressible liquid, J. Sound Vib. **277**, 163 (2004).
4 H. Sun, and O. M. Faltinsen, Water impact of horizontal circular cylinders and cylindrical shells, Appl. Ocean Res. **28**, 299 (2006).
5 P. Yu, H. Li, and M. C. Ong, Hydroelastic analysis on water entry of a constant-velocity wedge with stiffened panels, Mar. Struct. **63**, 215 (2019).
6 G. Zhang, S. Feng, Z. Zhang, Y. Chen, Z. Sun, and Z. Zong, Investigation of hydroelasticity in water entry of flexible wedges with flow detachment, Ocean Eng. **222**, 108580 (2021).
7 X. Zhu, O. M. Faltinsen, and C. Hu, Water entry and exit of a horizontal circular cylinder, J. Offshore Mech. Arctic Eng. **129**, 253 (2007).
8 Q. Qu, W. Rui, G. Hao, P. Liu, and R. K. Agarwal, in Numerical study of water impact of an elastic cylindrical shell using coupled FVM-FEM method: Proceedings of 54th AIAA Aerospace Sciences Meeting, San Diego, 2016.
9 L. B. Lucy, A numerical approach to the testing of the fission hypothesis, Astron. J. **82**, 1013 (1977).
10 S. Koshizuka, and Y. Oka, Moving-particle semi-implicit method for fragmentation of incompressible fluid, Nucl. Sci. Eng. **123**, 421 (1996).
11 Y. Zhang, D. Wan, and T. Hino, Comparative study of MPS method and level-set method for sloshing flows, J. Hydrodyn. **26**, 577 (2014).
12 Z. Tang, Y. Zhang, and D. Wan, Multi-resolution MPS method for free surface flows, Int. J. Comput. Methods **13**, 1641018 (2016).
13 X. Chen, and D. Wan, GPU accelerated MPS method for large-scale 3-D violent free surface flows, Ocean Eng. **171**, 677 (2019).
14 F. Xie, W. Zhao, and D. Wan, CFD simulations of three-dimensional violent sloshing flows in tanks based on MPS and GPU, J. Hydrodyn. **32**, 672 (2020).
15 B. H. Lee, J. C. Park, M. H. Kim, S. J. Jung, M. C. Ryu, and Y. S. Kim, Numerical simulation of impact loads using a particle method, Ocean Eng. **37**, 164 (2010).
16 Y. L. Zhang, Z. Y. Tang, and D. C. Wan, in Simulation of water entry of a free-falling wedge by improved MPS method: Proceedings of the Twenty-sixth International Ocean and Polar Engineering Conference, Rodos, 2016.
17 Z. Y. Tang, Y. L. Zhang, H. Z. Li, and D. C. Wan, in Overlapping MPS method for 2D free surface flows: Proceedings of the Twenty-fourth International Ocean and Polar Engineering Conference, Busan, 2014.
18 P. Sun, A. M. Zhang, S. Marrone, and F. Ming, An accurate and efficient SPH modeling of the water entry of circular cylinders, Appl. Ocean Res. **72**, 60 (2018).
19 A. Khayyer, and H. Gotoh, in A multi-phase compressible-incompressible particle method for water slamming: Proceedings of the Twenty-fifth (2015) International Ocean and Polar Engineering Conference, Hawaii, 2015.
20 R. Yan, J. J. Monaghan, A. Valizadeh, and F. Xu, The effect of air on solid body impact with water in two dimensions, J. Fluids Struct. **59**, 146 (2015).
21 S. C. Hwang, A. Khayyer, H. Gotoh, and J. C. Park, in Simulations of incompressible fluid flow-elastic structure interactions by a coupled fully Lagrangian solver: Proceedings of the Twenty-fifth International Ocean and Polar Engineering Conference, Kona, 2015.
22 A. Khayyer, H. Gotoh, H. Falahaty, and Y. Shimizu, An enhanced ISPH-SPH coupled method for simulation of incompressible fluid-elastic structure interactions, Comput. Phys. Commun. **232**, 139 (2018).
23 A. Khayyer, H. Gotoh, H. Falahaty, and Y. Shimizu, Towards development of enhanced fully-Lagrangian mesh-free computational methods for fluid-structure interaction, J. Hydrodyn. **30**, 49 (2018).
24 A. Khayyer, Y. Shimizu, H. Gotoh, and S. Hattori, Multi-resolution ISPH-SPH for accurate and efficient simulation of hydroelastic fluid-structure interactions in ocean engineering, Ocean Eng. **226**, 108652 (2021).
25 A. Khayyer, H. Gotoh, Y. Shimizu, and Y. Nishijima, A 3D Lagrangian meshfree projection-based solver for hydroelastic Fluid-Structure Interactions, J. Fluids Struct. **105**, 103342 (2021).
26 W. K. Sun, L. W. Zhang, and K. M. Liew, A smoothed particle hydrodynamics-peridynamics coupling strategy for modeling fluid-structure interaction problems, Comput. Methods Appl. Mech. Eng. **371**, 113298 (2020).
27 A. Khayyer, Y. Shimizu, H. Gotoh, and K. Nagashima, A coupled incompressible SPH-Hamiltonian sph solver for hydroelastic FSI corresponding to composite structures, Appl. Math. Model. **94**, 242 (2021).
28 Z. Qin, and R. C. Batra, Local slamming impact of sandwich composite hulls, Int. J. Solids Struct. **46**, 2011 (2009).
29 Y. H. Lu, G. Y. Zhang, and D. C. Wan, in Numerical simulations of an elastic plate entry water by coupled MPS-FEM method: Proceedings of International SPHERIC (SPH European Research Interest Community) Workshop, Harbin, 2020.
30 Z. Sun, K. Djidjeli, J. T. Xing, and F. Cheng, Coupled MPS-modal superposition method for 2D nonlinear fluid-structure interaction problems with free surface, J. Fluids Struct. **61**, 295 (2016).
31 G. Fourey, C. Hermange, D. Le Touzé, and G. Oger, An efficient FSI coupling strategy between smoothed particle hydrodynamics and finite element methods, Comput. Phys. Commun. **217**, 66 (2017).
32 N. Mitsume, S. Yoshimura, K. Murotani, and T. Yamada, Improved MPS-FE fluid-structure interaction coupled method with MPS polygon wall boundary model, Comp. Model. Eng. Sci. **101**, 229 (2014).
33 N. Mitsume, S. Yoshimura, K. Murotani, and T. Yamada, MPS-FEM partitioned coupling approach for fluid-structure interaction with free surface flow, Int. J. Comput. Methods **11**, 1350101 (2014).
34 Z. Zheng, G. Duan, N. Mitsume, S. Chen, and S. Yoshimura, A novel ghost cell boundary model for the explicit moving particle simulation method in two dimensions, Comput. Mech. **66**, 87 (2020).
35 Z. Zheng, G. Duan, N. Mitsume, S. Chen, and S. Yoshimura, An explicit MPS/FEM coupling algorithm for three-dimensional fluid-structure interaction analysis, Eng. Anal. Bound. Elem. **121**, 192 (2020).
36 T. Long, C. Huang, D. Hu, and M. Liu, Coupling edge-based smoothed finite element method with smoothed particle hydrodynamics for fluid structure interaction problems, Ocean Eng. **225**, 108772 (2021).
37 X. Chen, Y. Zhang, and D. Wan, Numerical study of 3-D liquid sloshing in an elastic tank by mps-fem coupled method, J. Ship Res.

63, 143 (2019).
38 G. Zhang, W. Zhao, and D. Wan, Partitioned MPS-FEM method for free-surface flows interacting with deformable structures, Appl. Ocean Res. **114**, 102775 (2021).
39 G. Zhang, R. Zha, and D. Wan, MPS-FEM coupled method for 3D dam-break flows with elastic gate structures, Eur. J. Mech.-B Fluids **94**, 171 (2022).
40 Y. Zhang, and D. Wan, MPS-FEM coupled method for sloshing flows in an elastic tank, Ocean Eng. **152**, 416 (2018).
41 M. Tanaka, and T. Masunaga, Stabilization and smoothing of pressure in MPS method by quasi-compressibility, J. Comput. Phys. **229**, 4279 (2010).
42 B. H. Lee, J. C. Park, M. H. Kim, and S. C. Hwang, Step-by-step improvement of mps method in simulating violent free-surface motions and impact-loads, Comput. Methods Appl. Mech. Eng. **200**, 1113 (2011).
43 A. Khayyer, H. Gotoh, and S. Shao, Enhanced predictions of wave impact pressure by improved incompressible SPH methods, Appl. Ocean Res. **31**, 111 (2009).
44 N. M. Newmark, A method of computation for structural dynamics, J. Eng. Mech, Div. **85**, 67(1959).
45 K. M. Hsiao, J. Y. Lin, and W. Y. Lin, A consistent co-rotational finite element formulation for geometrically nonlinear dynamic analysis of 3-D beams, Comput. Methods Appl. Mech. Eng. **169**, 1 (1999).

MPS-FEM耦合方法数值仿真弹性圆柱砰击自由液面的水弹性响应问题

黄聪祎, 张冠宇, 万德成

摘要 在船舶工程和海洋工程领域中, 结构入水是一个典型的流固耦合问题. 在入水过程中, 结构物与流体砰击引起的水弹性效应引起了研究人员的广泛关注. 在本文中, 采用MPS-FEM耦合方法求解流固耦合问题. 其中, MPS方法非常适用于模拟剧烈的自由表面流动, FEM方法在求解结构的变形时的准确性和鲁棒性较高. 本文发展MPS-FEM耦合方法, 数值仿真分析了圆柱砰击流体自由表面时的水弹性响应问题. 首先对刚性圆柱的入水过程进行了数值计算, 所得结果与已有文献数据吻合较好. 接着对弹性圆柱入水过程进行模拟, 分别对结构弹性和冲击速度进行了变量分析.